Bioinspired hierarchical ceramic sutures for multi-modal performance

Katz, Zachary; Yazdani Sarvestani, Hamidreza; Gholipour, Javad; Ashrafi, Behnam

Publisher's version / Version de l'éditeur:
https://doi.org/10.1002/admi.202300098
Advanced Materials Interfaces, 10, 14, 2023-04-07

ADVANCED MATERIALS INTERFACES
Open Access
www.advmatinterfaces.de

Bioinspired Hierarchical Ceramic Sutures for Multi-Modal Performance

Zachary Katz, Hamidreza Yazdani Sarvestani, Javad Gholipour, and Behnam Ashrafi**

Natural suture structures, characterized by hard segments joined along a patterned weak interface, are found to provide unique toughening mechanisms for brittle bulk biological materials. Hierarchical ceramic sutures inspired by white-tailed deer crania and diabolical ironclad beetle exoskeletons are developed using a biomimetic approach. Overlapping geometries unlock twin energy absorption mechanisms. Ceramics with Surlyn-infiltrated precision laser-cuts are fabricated using a semi-automated and smart advanced manufacturing platform. A parametric study comprising four-point bending, fracture toughness, and tensile tests is conducted to evaluate toughness, strength, and stiffness with geometrical interlocking in two hierarchical orders. Digital image correlation is utilized to analyze the local toughening mechanisms and failure modes in the fracture tests. For all three metrics, the panels with second-order hierarchy outperform the anti-trapezoidal equivalents. The ceramic sutures show up to 590%, 340%, and 700% improvements in energy absorption in the tensile, bending, and fracture tests, respectively, owing to the optimal first- and second-order interlocking angles. The high-order fractal interlocking at multiple scales and overlapping teeth are found to provide high flexibility and failure resistance, whereas progressive fracture mechanisms delay catastrophic failure by up to 50%. The concept of hierarchical suture can lead to industrially applied ceramic systems with tailored mechanical performances.

1. Introduction

Biomimicry refers to the design of systems inspired by those found in nature. Biomimetic structures utilize segmentation, rotation, layering, and more, in the same manner as nature to emulate biological behavior.[1] These structures have been classified into eight categories: overlapping, fibrous, helical, gradient, layered, tubular, cellular, and suture structures, each of which is suitable for unique applications (**Figure 1**a).[1,2] Structural hierarchy is frequently observed in nature as a method of combining, amplifying, or balancing mechanical properties. For instance, bone is a lightweight, fracture-resistant material with features of different length scales.[3] Conversely, tessellating geometries through hierarchical length scales can be used to tune the properties of engineering materials.[4] For example, patterning a structure at different length scales in a fractal manner has been shown to influence the mechanical properties and failure response.[5,6]

The high strength, stiffness, and thermal and chemical resistance of engineering ceramics make them desirable for a plethora of applications (Figure 1b). Architected ceramics with precise cut geometries have been widely used in automobile engines, heat exchangers, and aerospace applications.[7] Due to the extremely brittle nature of ceramics, there are significant drawbacks to traditional contact machining. Ultrashort-pulse laser ablation is a highly attractive option, as it solves most of these issues by offering a high-precision non-contact method. The tunability of the strength, toughness, stiffness, and failure mechanism of ceramics is of particular interest to researchers.[8–13] This tuning is primarily accomplished through segmentation or engraved continuous geometries that can be infiltrated with soft polymers.[14–17] The polymer acts as an adhesive interlayer, reducing localized stresses and guiding cracks through weaker cut interfaces.[8,18]

Across domains, hard biological features of organisms, such as beetle exoskeletons,[19] turtle osteoderms,[20] diatom frustules,[1] and mammalian skulls,[21] exhibit patterned interdigitating teeth with soft interfaces (Figure 1c,d). These structures, known as sutures, allow hard structures to dissipate large amounts of energy before failure, occasionally offering progressive fracture mechanisms to prevent catastrophic failure. Sutures functionally facilitate growth and joint mobility and are central to many organic structures.[22] Generally speaking, the greater the level of interdigitating, the more energy the structure can dissipate.[21] Mammalian cranial sutures and ammonite (triangular teeth) (see Figure 1b), some of the most complex, interdigitated sutures found in nature, have been extensively studied.[21,23–28] These engineered sutures have been

Z. Katz, H. Yazdani Sarvestani, J. Gholipour, B. Ashrafi
Aerospace Manufacturing Technology Center
National Research Council Canada
5145 Decelles Avenue, Montreal, QC H3T 2B2, Canada
E-mail: hamidreza.yazdani@nrc-cnrc.gc.ca; behnam.ashrafi@nrc-cnrc.gc.ca

The ORCID identification number(s) for the author(s) of this article can be found under https://doi.org/10.1002/admi.202300098.

DOI: 10.1002/admi.202300098

ADVANCED MATERIALS INTERFACES
Open Access
www.advmatinterfaces.de

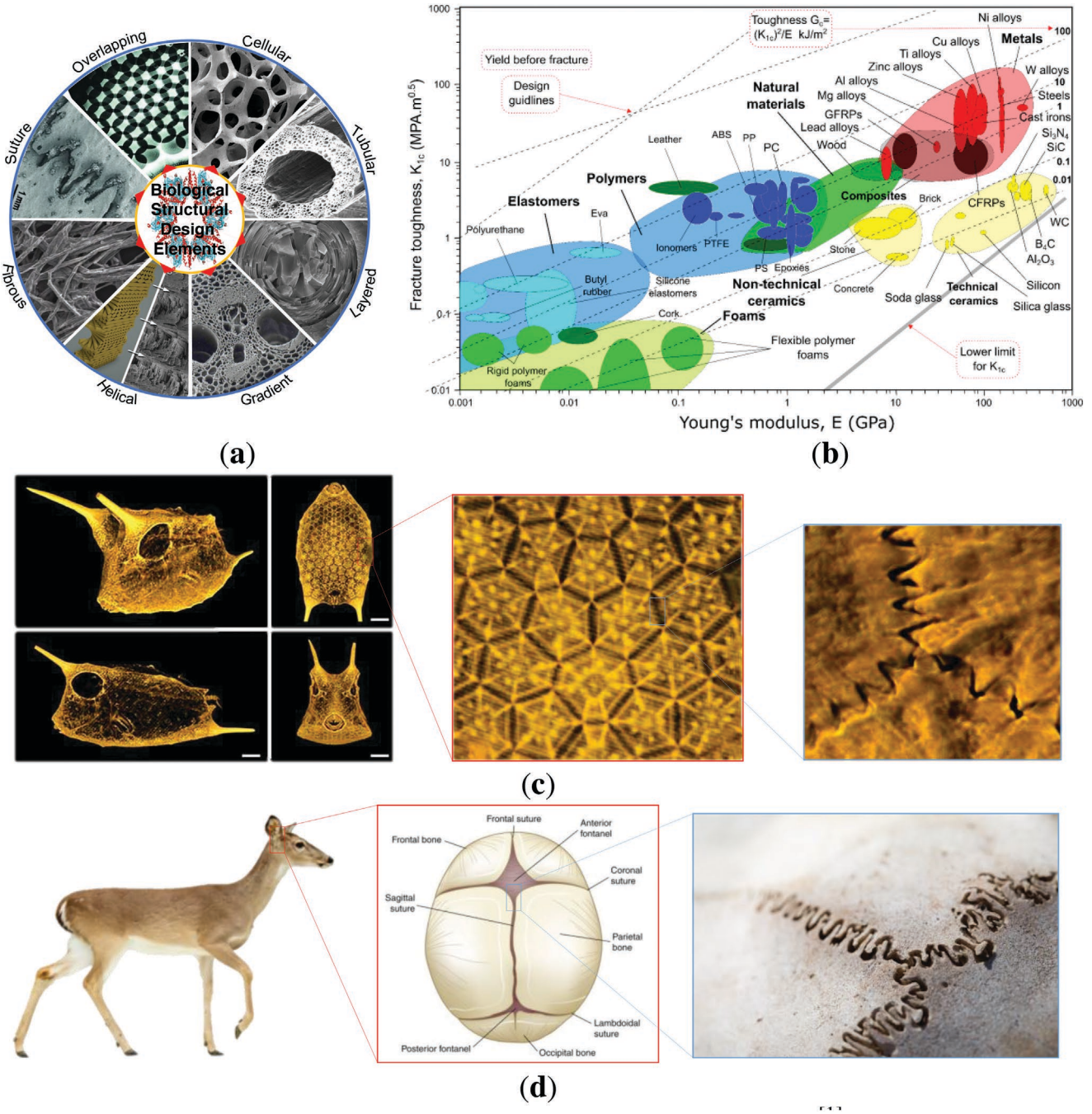

Figure 1. a) Common biological structures mimicked in engineering.[1] b) Fracture toughness versus Young's modulus: (recreated based on similar charts by Ashby). c) The boxfish gets its name from its boxy shape (left). Its carapace (or shell) is composed of several hexagonal scutes that provide body support and armored protection (center). These scutes are connected by tooth-like joints called sutures, which provide some level of combined strength and flexibility (right). d) White-tailed deer (mammalia) with cranial sutures.

thoroughly modeled and tested, with a variety of geometries and materials being considered. These materials are of great interest for toughening ceramic joints in multiple modes.[27] When focusing on rounded geometries with tunable pullout characteristics,[9,10,18,29,30] joints, often composed of frictional interfaces (rather than polymer filled), use the interlocking angle to manipulate toughness and stiffness while avoiding fracture, which would abruptly interrupt the interfacial energy dissipation.[18] Although a few joinery studies have been performed on metallic or glassy interfaces and their composition for high-temperature applications up to matching the mechanical properties of the bulk,[31–33] less attention has been paid to industrial-scale manufacturing platforms to fine-tune overall mechanical performance, such as stiffness, strength, and (fracture) toughness, based on a weak architectured interface.

In this study, a novel hierarchical ceramic suture of mixed architectures, inspired by the white-tailed deer and diabolical ironclad beetle, was engineered to improve the strength and toughness and fine-tune the stiffness and deformability across multiple modes. The high-order fractal geometrical interlocking at multiple scales and overlapping teeth provides high flexibility and failure resistance, whereas progressive fracture mechanisms delay catastrophic failure in flexure, tension, or notched fracture scenarios. A digital manufacturing platform was used to fabricate defect-free hierarchal interlocking teeth with high precision. This study can guide the design and manufacture of ceramic joints for low- and high-temperature applications by highlighting the value of the weak interface while allowing ceramic joints to preserve their structural integrity at much higher temperatures.

2. Results

This paper is organized as follows: Section 2.1 discusses the strength, stiffness, and energy absorption of suture systems subjected to tensile loading. Section 2.2 presents the mechanical performance of the sutures under four-point bending. In Section 2.3, the fracture properties of the suture systems have been explored. Section 3 discussed all the results from three loading conditions and compare them with the available data in the literature. Section 5 describes the sample characterization, manufacturing, and experimental setups.

2.1. Tensile Loading

Tensile strength, stiffness, and energy absorption were evaluated through uniaxial loading, as shown in **Figure 2**. Each sample demonstrated comparable failure mechanisms, except for the 15°-25° sample, which exhibited a large progression until failure, characteristic of failure of one side of the ceramic. Looking closely at the force-displacement curves (see Figure S1, Supporting Information), small drops in force can be observed, attributed to progressive failure for most samples, which is clearly illustrated by the 25°-5° and 25°-35° samples. Unlike the bending samples, progressive failure does not significantly decrease the strength. The tensile force-displacement curves also illustrate a low initial modulus characteristic of the contact followed by stiffening of the samples with increasing displacement. The samples exhibiting only the *N1* suture system were among the least stiff and least strong, similar to other loading modes. For some suture systems, geometrical hardening along

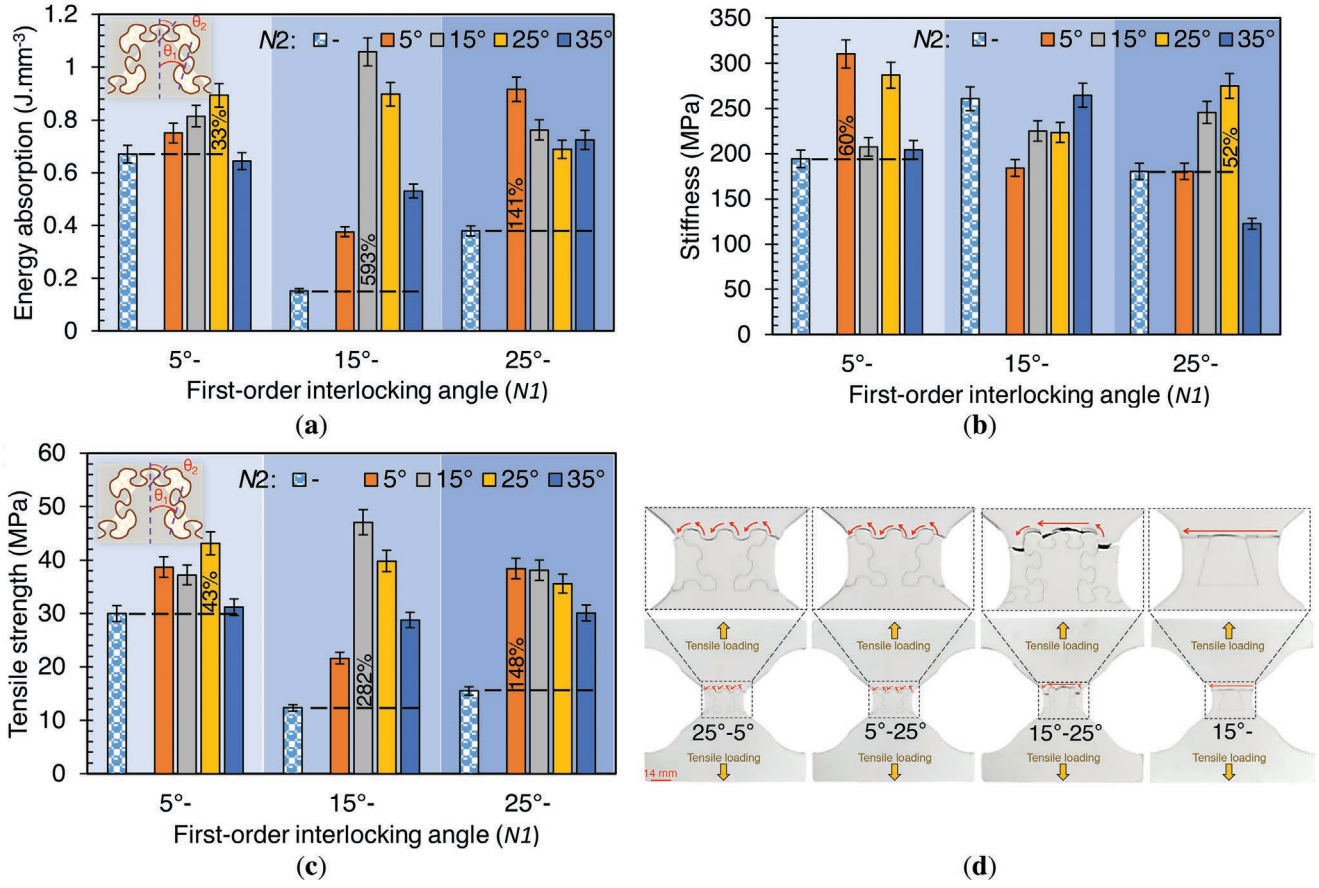

Figure 2. Tensile properties of the ceramic sutures: a) energy absorption, b) stiffness, and c) tensile strength where θ_2 (*N2*) = 5°, 15°, 25°, or 35° and θ_1 (*N1*) = 5°, 15°, or 25°. d) Crack deflection, tooth pullout/fracture in the tensile samples: 25°-5°, 5°-25°, 15°-25°, and 15°- sutures.

with progressive interlocking is strong enough for deformation to spread within the weak interfaces. Tooth pullout/fracture eventually occurred, resulting in a sharp drop in the force.

As shown in Figure 2a, the optimal *N2* interlocking angles for *N1* = 5°, 15°, and 25° are *N2* = 25°, 15°, and 5°, respectively. The *N2* interlocking angle causes the suture system to have a higher energy absorption capability. Therefore, with increasing *N1* interlocking angle, the optimal *N2* interlocking angle decreases. This is because when *N1* and *N2* interlocking angles are both too high, the tooth pullout process was prematurely interrupted by the tooth fracture, leading to low energy absorption, as shown in Figure 2d. The energy absorption increased with the *N2* interlocking angle for the 5°- sample up to 5°-25° where it decreased. Similarly, the 15°- set showed a peak at 15°-15°, the absolute toughest sample with a sevenfold increase over the *N1*-only sample. For the 15°- suture, tooth fracture/cracking occurred during the pullout process, with more unexpected and brittle failures. The 25°- set showed a general decrease in energy absorption with an *N2* interlocking angle, following the trend of decreased properties with increasing *N2* interlocking for this set. The 5°- suture exhibited impressive energy absorption, even surpassing the 5°-35° suture; however, introducing a geometric hierarchy generally improved the energy absorption of a sample. The 25°-5° sample further offered a 141% improvement over the 25°- sample (minimal interlocking and low frictional resistance). Finally, the 5°- samples exhibited a nearly linear increase in energy absorption up to their maximum at 5°-25°. The 5°-5° and 5°-25° samples were the stiffest, exhibiting 60% and 50% greater stiffnesses than the *N1* sample, respectively, as shown in Figure 2b. The 15°- sample exhibited a relatively high stiffness, outperforming many of the *N2* samples. However, the 15°-35° sample was still stiffer. There appears to be a potential correlation between *N2* interlocking angle and stiffness, particularly for *N1* of 15°- and 25°-; however, for the 25°- sample, there was an optimal stiffness before it dropped off owing to the substantial damage to the teeth, leading to interrupted early pullout. Depending on the failure mechanism, the tensile strength correlated with the stress at the soft interlayer failure (resulting in rough surfaces), tooth failure (brittle with smooth surfaces), or both simultaneously, whichever occurred first. In the case of soft interlayer failure, there might be some changes in the tensile strength owing to the failure mechanisms of the weak interface, controlled by the ratio of normal stress to shear stress of the soft phase (the stretching and shearing modes). The first-order suture systems failed mostly through soft interlayer failure, whereas for the second-order suture systems, *N1* and *N2* interlocking tooth failure at the base of the teeth both played a role in the failure mechanisms. Improvements in tensile strength were exhibited for all three geometry groups (*N1*-*N2* sutures where *N1*: 5°, 15°, 25°, and *N2*: 5°, 15°, 25°, and 35°) over the baselines (i.e., *N1* sutures). While the 5°- sample exhibited greater strength than some of the hierarchical samples, it was surpassed by all 5°- hierarchical samples in its category. For the 5°- sutures, no appreciable trend was observed; however, the 15°- sutures showed a peak at *N2*: 15°, while the 25°- samples showed increasing strength with decreasing *N2* interlocking angle (see Figure 2c). The 15°-15° sample exhibited the highest tensile strength (caused by tooth pullout), with a 280% improvement over the 15°- sample. For the 15°-15° sample, crack growth was a progressive and stable mechanism involving tooth pullout, along with interlocking stresses and frictional dissipation. The 5°-25° sample, competing with the relatively high-performance 5°- sample, still offered an increase in strength of 40%. The effect of the soft material (i.e., Surlyn interlayers) in the suture system is to redistribute high stresses across the weak interfaces to suppress the fracture of the solid parts (i.e., ceramic) of the system. These high stresses are generated because the interactions between the teeth depend on the frictional contact. In addition, infiltrated soft interlayers render extreme designs (i.e., higher interlocking angles) more accessible, leading to more encouraging combinations of strength and energy absorption.

2.2. Four-Point Bending

To evaluate the impact of suture geometry on strength, stiffness, and energy absorption, 15 suture samples (Figure 8g) were tested in the flexure. **Figure 3** shows the bending properties of the ceramic sutures. The samples exhibiting only one order of hierarchy (e.g., 5°-) performed worse in terms of both strength and flexibility than all *N2* samples having two orders of hierarchy. The 5°- sample exhibited sudden, catastrophic failure, whereas the 15°- and 25°- samples exhibited some progressive failure in the major anti-trapezoidal teeth (see Figure S2, Supporting Information). In contrast, all the samples with two orders of hierarchy demonstrated high levels of progressive failure, as shown in Figure 3d. In all cases, after an initial drop in load owing to crack initiation, the sample reattained the same stiffness, with this pattern repeating in a sawtooth pattern until catastrophic failure occurred. This demonstrates the flaw tolerance of the design, as the initial localized failures do not negatively impact the overall performance. This also allows the parts to flex up to one millimeter from the initial crack (in the 5°-5° configuration) before failure, offering 2.5 times greater flexibility than the base 5°- sample. Continuing to focus on these two samples, a large drop in load was observed following crack initiation for the 5°-5° sample, which occurred at nearly the same displacement as that of the 5°- sample. This suggests that a major tooth fracture was responsible. With the ability to control the sequence of the teeth at different length scales, fractures can provide unique design opportunities for these materials. In terms of ultimate flexural strength (UFS), the *N2* joints again outperformed the *N1* geometries by a significant margin (Figure 3c). For the samples with an *N1* interlocking angle of 5°, a near-linear increase in strength with *N2* interlocking angle was observed. For the 15° samples, the UFS generally increased with the *N2* angle; however, the 25° samples demonstrated a much less significant dependence on the geometry. The UFS results show that *N1* interlocking angle is much more relevant to the flexural performance, indicating that first-order tooth fracture has a significantly greater role in its failure mechanism. The weaker dependency on the second-order suture geometry for the 25°- set can be attributed to the narrower first-order tooth neck width. Referring to **Figure 4**, the extreme difference in the first-order interlocking tooth neck between a 5° or 15° sample versus a 25° one in terms of *N1* hierarchy is apparent, as shown in Figure 8e. This

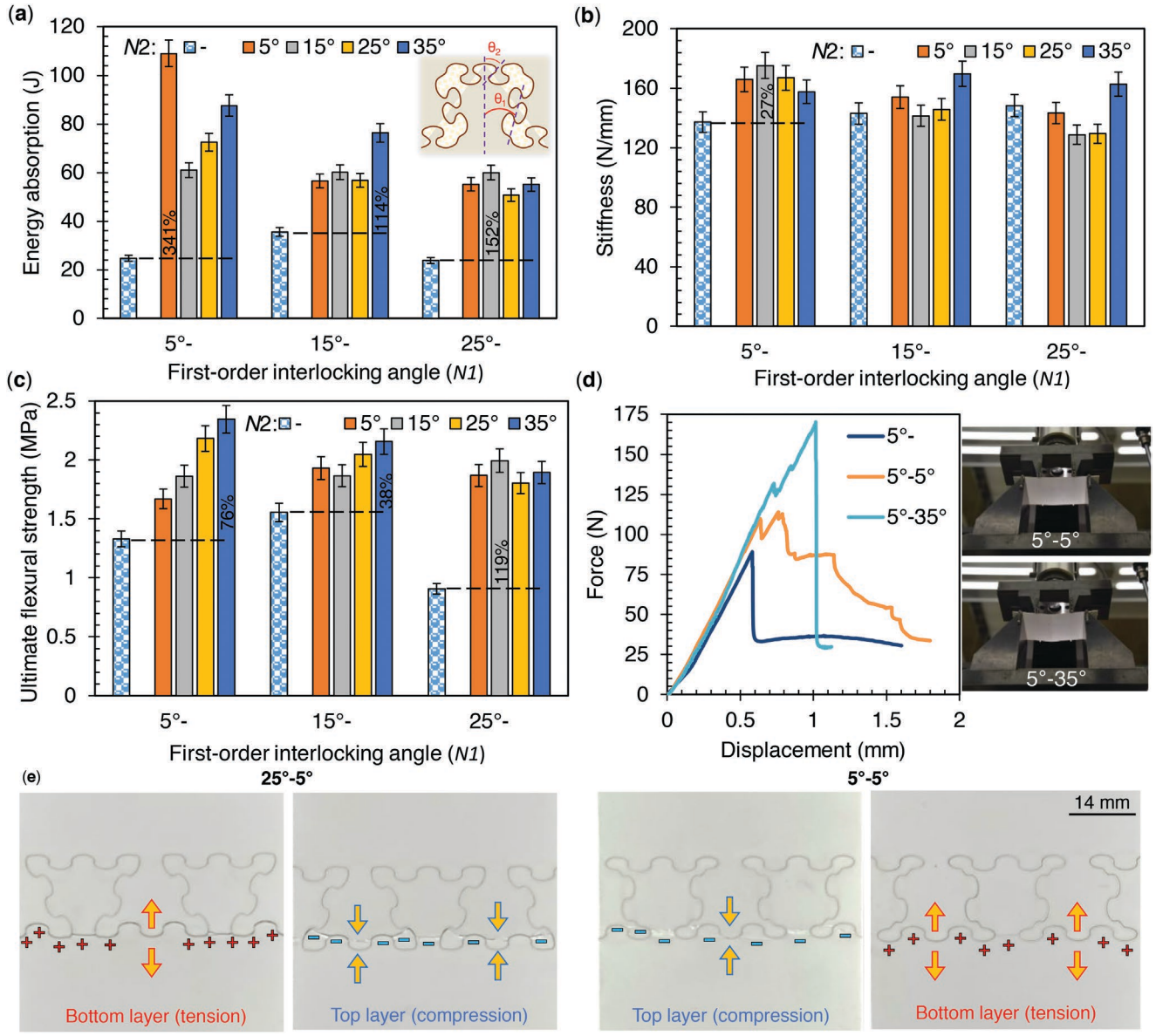

Figure 3. Bending properties of the ceramic sutures: a) energy absorption, b) stiffness, and c) ultimate flexural strength where θ_2 (*N2*) = 5°, 15°, 25°, or 35° and θ_1 (*N1*) = 5°, 15°, or 25°. d) Force-displacement curves where θ_2 (*N2*) = 5°, 35°, and θ_1 (*N1*) = 5°. e) The top and bottom layers of the 25°-5° and 5°-5° ceramic sutures subjected to a four-point bending load.

is of high importance because there is less load-bearing material where the stress is concentrated at the tooth necks, which could explain why *N2* interlocking angle is less relevant to its failure characteristics. This is further validated by finite element analysis study on the 15°- and 25°- sets described in Supporting Information (Figures S4 and S5, Supporting Information), where all samples but the 15°-35° and 25°-35° sutures showed maximum stress in the first-order interlocking tooth region. This reinforces the hypothesis that first-order interlocking tooth fracture is the dominant failure mechanism for these samples, especially considering the extremely narrow second-order interlocking tooth neck widths of the -35° samples, failing early and at considerably lower stress. In all cases, the addition of a second-order hierarchy increased the strength. Notably, the dovetail sample with 15° interlocking angle exhibited the best UFS among the non-hierarchical samples. The stiffness, on the other hand, showed few trends, with relatively good performance compared to the anti-trapezoidal samples. There was a slight increase in stiffness with an *N1* interlocking angle for the anti-trapezoidal samples and a slightly decreasing trend for the hierarchal samples with *N2* interlocking angles of 15° and 25° (see Figure 3b). The highest and lowest stiffnesses were exhibited by samples with an *N2* interlocking angle of 15°, exemplifying the sensitivity of stiffness to geometric manipulation of the design. The 5°-25° sample was likely the least stiff because of the relatively narrow necks of the anti-trapezoids in this configuration. For the 5° set, a peak is observed at 15°. The 5°-15° and 15°-35° samples exhibited the greatest stiffness,

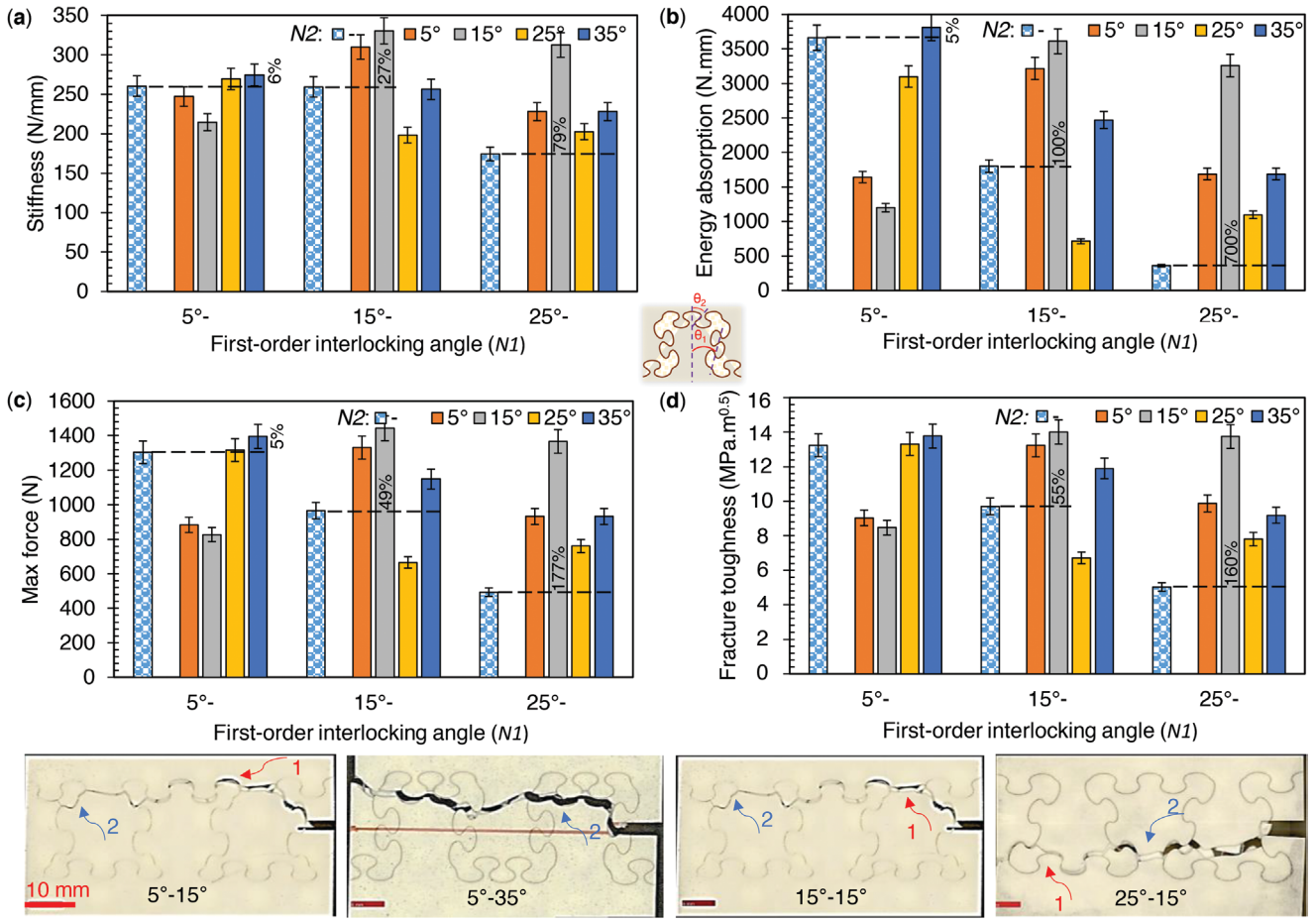

Figure 4. Fracture properties of the ceramic sutures: a) stiffness, b) energy absorption, and c) maximum force. d) Fracture toughness where θ_2 (*N2*) = 5°, 15°, 25°, or 35° and θ_1 (*N1*) = 5°, 15°, or 25° (Number 1: tooth pullout, and Number 2: tooth failure).

offering a 25% increase over *N1* samples. Looking across the sample sets discussed herein, increasing the interlocking angle to the extremes appears to benefit stiffness in most cases. Across all hierarchical samples, the energy dissipation was inversely correlated with *N1* interlocking angle. This can be attributed to the 5°- samples having generally good flexibility without sacrificing strength or stiffness compared to the other sets. The best samples, the 5°-5°, and 5°-35° sutures exhibited the highest and second-highest energy dissipations of all tested samples. Consequently, lower *N1* interlocking angles are better suited for applications in which high flexural toughness is desired. Furthermore, these samples exhibited some of the best and worst flexural strengths, indicating no correlation between the strength and energy dissipation. The 5°-5° sample, which exhibited the most extreme progressive and delayed failure, was an outlier among all samples. It is observed that with a suitable set of interlocking angles, the effective teeth pullout mechanism is functional, resulting in a stable system and progressively decreasing force with the crack opening. Among those tested, the samples with only one order of hierarchy exhibited significantly worse energy dissipation (Figure 3a). This can be attributed to cracks forming primarily along straight horizontal lines, propagating through the necks, and extending to the edges, resulting in premature failure. It could be of great use to investigate lower orders of *N1* interlocking angles in hierarchical samples to determine the limits of the samples' ability to delay failure. Within the *N1* set, no trend in terms of energy dissipation could be extrapolated, although the 5°-35°, 15°-35°, and 25°-35° samples were the best or second best of their sets. Therefore, it can be concluded that there is a slight increase in energy dissipation with an *N2* interlocking angle. The 15°-15° and 25°-15° samples were also the best or second best in their sets, indicating that the 15° of *N2* interlocking angle offers good dissipation in certain hierarchical cases. The 15°-25° and 25°-25° samples both exhibited very little progressive failure (one or two cracks before catastrophic failure), making the 25°- samples some of the worst in terms of flaw tolerance. This parallels how the anti-trapezoidal samples failed, 25°- sample exclusively, with virtually no further extension after the initial crack formation. In summary, samples with a variety of *N2* tooth shapes appeared to perform best, while those with similar corners and central teeth appeared to underperform. This is likely due to the variance in neck width, resulting in sacrificial teeth dissipating energy early. Similar to tensile strength, the soft interlayers and their energy dissipation capability (due to plastic deformation) have considerable effects on the overall toughness of these suture systems in the four-point bending condition. During the four-point bending test, the top suture layer was

subjected to compressive load, whereas the bottom suture layer was subjected to tensile load. It is observed that the bottom layer failed first owing to the deflection of cracks through the weak interfaces, forcing the top layer to fracture, which is not necessary for the designed interface of the top layer (see Figure 3e). The anti-trapezoidal sample with an interlocking angle of 15° demonstrated the best energy dissipation of the dovetail samples (along with its high strength), in agreement with other studies that found it to be the optimal angle for pullout without fracture.[18,19,30]

2.3. Narrow Notch Side-Loaded In-Plane Fracture

The notched fracture-tested samples exhibited rapid and instantaneous crack propagation compared to those tested in bending. This was attributed to the relatively fast displacement rate (5 mm s^{-1}) and crack-guiding effects of the notch. A baseline sample exhibiting one order of hierarchy was used to benchmark the improvements in toughness and energy absorption. Figure 4 presents the fracture properties of the ceramic sutures including stiffness, maximum force, energy absorption, and fracture toughness. The 5°-25° suture system exhibited the highest stiffness. This improvement in stiffness compared to its first-order baseline is due to the contribution of an increased load transfer to the second-order interlocking teeth. This increase in load transfer to the teeth can be visualized by experimental digital image correlation (DIC) contours, as shown in **Figure 5**, by comparing the contours before and after failure. Therefore, the improvement in the stiffness of each ceramic suture system (i.e., θ_1 (*N1*) = 5°, 15°, and 25°) is dependent on *N1* interlocking angle and second-order tooth geometry, where the higher the *N1* interlocking angle, the more significant is the increase in the stiffness improvement, as shown in Figure 4a. It can be observed that with an increasing *N1* interlocking angle, the stiffness decreases. This is because tooth failure is expected to occur in suture systems with high-stress concentrations at the base of the teeth owing to the smaller cross-sectional area. The higher the *N1* interlocking angle, the smaller the cross-sectional base area. Suture systems that fail by tooth failure are more brittle and catastrophic with much less energy absorption capability, resulting in lower fracture toughness. As shown in the DIC images in Figure 5, the more interlocked *N1* samples channeled strain toward the corners of the teeth, which in extreme cases caused a fracture to originate away from the notch (whereas in other cases, tooth pullout was the dominant failure mode). This is logical because the length between the corner of the anti-trapezoid and the edge of the sample is less than the overall length of the notch. Interestingly, the 5°- sample absorbed the second-highest energy of all the samples tested, although its fracture toughness was closer to the average. The anti-trapezoidal data demonstrated a clear inverse correlation between *N1* interlocking angle and performance. Because the least-interlocking sample provides the least resistance to vertical motion, the friction occurring at the interlocking interface can dissipate high amounts of energy. However, the motion/sliding at this interface is why the fracture toughness, which is dependent on the slope of the load-displacement curve, is lower than that of some of the other samples. If the 15°- and 25°- were designed such that failure was guaranteed to occur at the notch, they would likely test better, as this factor had a significant impact on their overall performance. Looking at the hierarchical samples, the 15°-15° sample proved to be the toughest with the sign of stable crack propagation, as seen in Figure 5, demonstrating 60% greater fracture toughness than the baseline, with the second-best energy absorption of the set. As shown in Figure 5, the crack followed the entire length of the weak interface during a progressive and stable process. In this design, the pullout mechanisms overcome the ceramic fracture. Samples exhibiting a 15° of *N2* interlocking angle generally performed well. The 5°-35° sample absorbed 140% more energy than the baseline (see Figure 4b), offering the second-best fracture toughness (aside from the 5°- sample). As previously discussed, 15° has been validated as the optimal angle for frictional pullout without fracture (a condition for a crack deflection into weak interfaces),[18,19,30] which corresponds to higher strength and energy absorption. In the side-loaded mode of fracture testing, the energy dissipated at these interlocked interfaces contributed to the toughness and energy absorption capability of the best samples. The 5°-35° sample, which performed well under multiple loading conditions, balanced the high and low interlocking in a complex manner, dividing them among different hierarchy orders. Notched fracture testing resulted in the highest fracture toughness, as the high interlocking of the *N2* teeth offered significant resistance to displacement, whereas the *N1* angle of 5° offered the widest base of the teeth and hence resistance to crack propagation (a brittle fracture). Considering that the 5°-25° suture system was a good performer, but the 15°-25°, 25°-25°, and 25°-35° systems performed less well (short series of stable crack growth), this theory is supported by the data.

Therefore, the interlocking angle and order of the structural hierarchy impart the ability to tune the fracture toughness of suture structures to deflect and guide propagating cracks in a stable fashion. Although the cracks can initially propagate along weak interfaces, the second-order hierarchy can make crack propagation challenging. Therefore, the cracks became progressively trapped as they propagated, leading to an increase in overall toughness.

3. Discussion

Utilizing the developed digital manufacturing platform to precisely control the hierarchical interlocking of the architected sutures, a ceramic composite with significantly enhanced energy absorption and deformability has been developed. This automated manufacturing method facilitates the exploration of both the extrinsic (behind the crack tip) and intrinsic (ahead of the crack tip) toughening mechanisms, each contributing to the energy absorption of the developed ceramic suture systems. These mechanisms include plastic deformation in adhesive interlayers, inter-tooth sliding (i.e., frictional energy dissipation), frictional tooth pullout, delamination in adhesive interlayers and ceramic tiles, crack deflection, and ceramic tooth fracture.

Figure 6a,b illustrates the force-displacement curves for the 5°-35° and 25°-35° ceramic sutures in the side-notched

ADVANCED MATERIALS INTERFACES
Open Access
www.advmatinterfaces.de

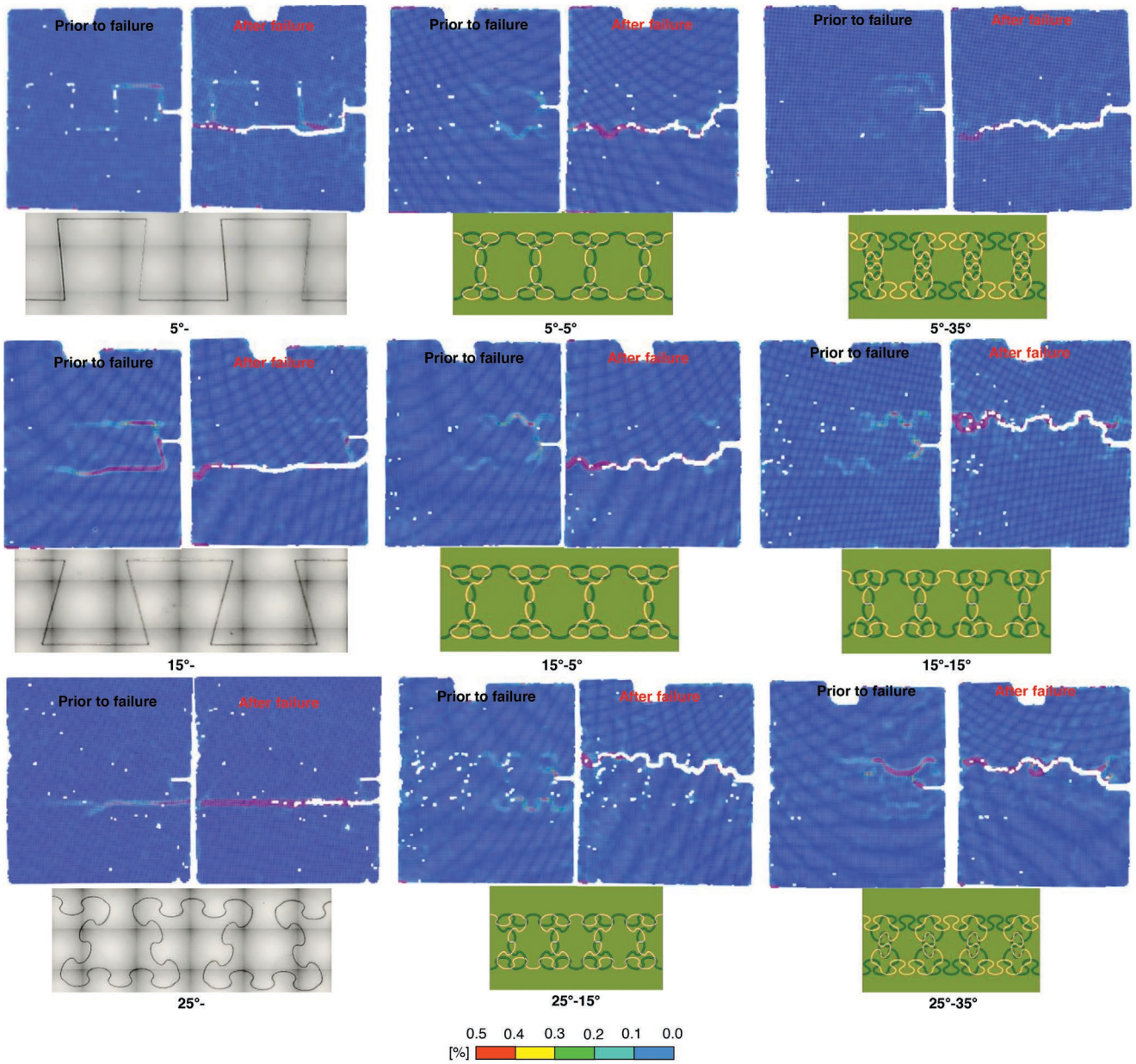

Figure 5. Experimental displacement contours of the ceramic sutures using digital image correlation for the fracture immediately prior to and after the failure where θ_2 (*N2*) = 5°, 15°, or 35° and θ_1 (*N1*) = 5°, 15°, or 25°.

fractures. Both sutures deformed and failed via similar mechanisms (Figure 6b); however, *N1* interlocking angle significantly contributed to the performance. For the 5°-35° suture, the force dropped at a higher maximum load and displacement than for the 25°-35° suture. The force-displacement data revealed two distinct phases of deformation. In phase I, the force increased with the displacement. Small drops may occur owing to the damage between the teeth; however, the force continues to increase in this phase owing to tooth interlocking. Phase I was characterized by no observed damage in the adhesive interlayer and no visible separation in the adjacent interlocking teeth. Phase II follows the failure of the first tooth (as well as damage to the adhesive interlayer), owing to the localized deformation and stress concentration near the tooth tip (reaching the peak load). A significant drop in force occurred when the rest of the suture structure could not carry the load. In this phase, the suture can still carry a lower load level up to complete failure owing to tooth failure or frictional pull-out. Mixed failure mechanisms were observed at the weak interface during Phase II.

Figure 6c–e presents the material performance with respect to toughness as a function of stiffness for all suture designs for tensile, bending, and fracture modes. The second-order hierarchy in the architected systems leads to reduced stiffness and high deformability when compared to those with only one order of hierarchy. This could be an advantage for flexible protection applications (e.g., personnel protective equipment).

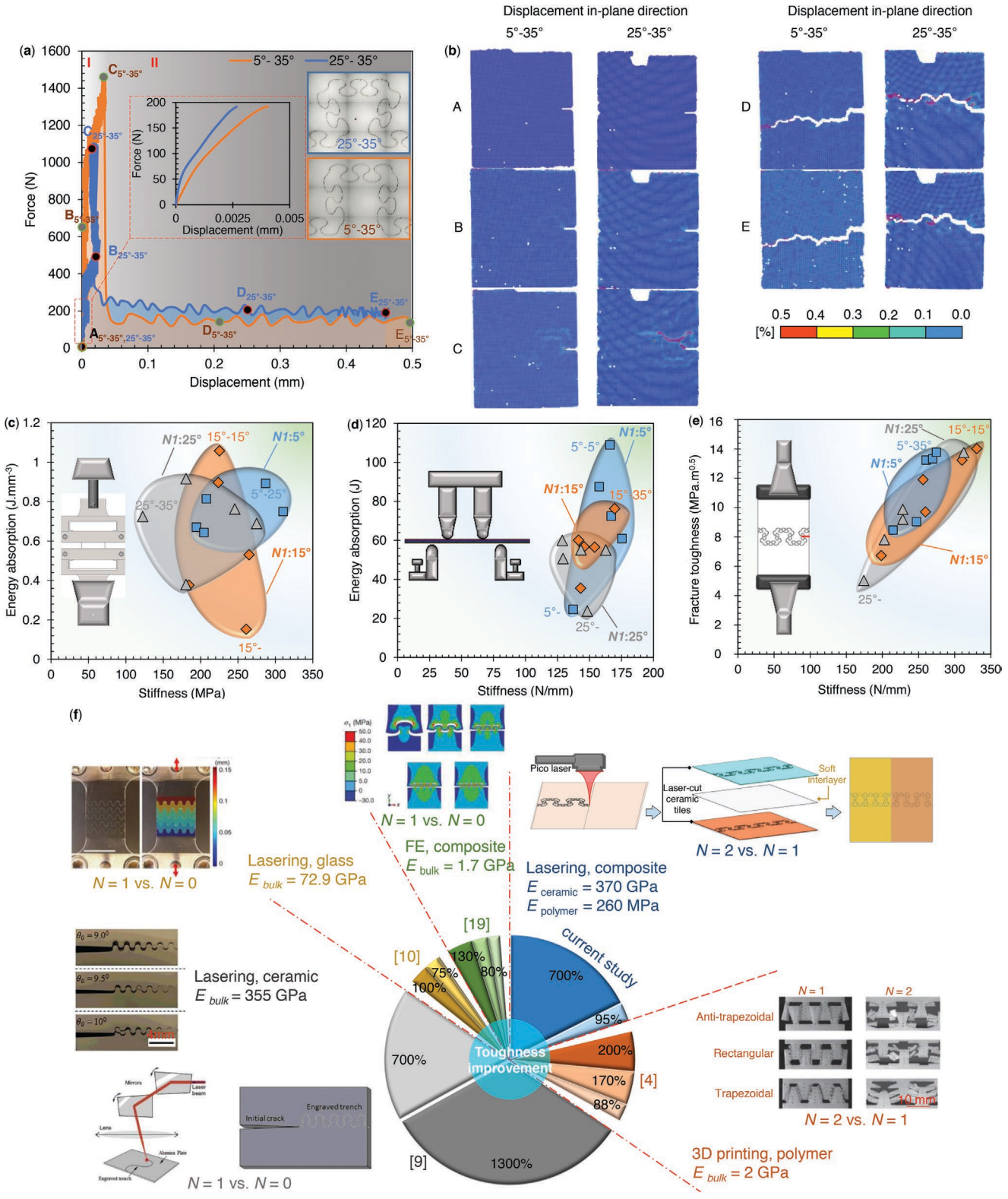

Figure 6. Fracture of the 5°-35°, and 25°-35° ceramic sutures: a) the force-displacement curves, b) the in-plane displacement field at five stages of the loading. Comprehensive material performance of ceramic sutures where θ_2 ($N2$) = 5°, 15°, 25°, or 35° and θ_1 ($N1$) = 5°, 15°, or 25° in a toughness versus stiffness plot: c) tensile, d) bending, and e) fracture. f) Toughness improvement of the current study compared to the suture architectures with similar processing techniques and geometries in literature.[4,9,10,19]

Table 1. Best two ceramic sutures of each testing category.

Testing Mode	Tensile		Bending		Fracture	
Property						
Energy absorption	15°-15°	25°-5°	5°-5°	5°-35°	5°-35°	5°-
(Fracture) Toughness	15°-15°	25°-5°			15°-15°	5°-25° 15°-25°
Strength	15°-15°	5°-25°	5°-35°	5°-25°		
Maximum force					15°-15°	5°-35°
Stiffness	5°-5°	25°-5°	5°-15°	15°-35°	15°-15°	25°-15° 5°-15°

Figure 6e illustrates how the sutured ceramics offer up to a 358% improvement in energy absorption (fracture mode) in comparison to its baseline, which is significant for applications where energy must be dissipated.

Through the precise geometry control afforded by the advanced manufacturing system, the toughness, stiffness, and strength properties can be tuned for target engineering and armor applications. For instance, personnel protective equipment must be less stiff (to provide comfort). These properties are achieved by selecting a higher-order hierarchy and tuning the *N2* interlocking angle without compromising the surface hardness and durability of the ceramic material. To further summarize the tunability of the overall mechanical behavior of the ceramic sutures, the two best sutures for each testing category are listed in **Table 1**. It is demonstrated that with energy dissipation in mind, the 15°-15° ceramic suture is the best energy-dissipating candidate with high energy in the tensile and fracture modes, whereas the 5°-5° configuration is optimal in flexure. This agrees with previous studies on suture structures, which have identified 15° as the critical angle for pullout without fracture in tensile or fracture modes.[18,19,30]

Figure 6f illustrates the toughness improvement comparison of the current study with the suture architectures in the literature using similar processing techniques such as laser removal systems and 3D printing. In addition to the current study and ref. [4], where the toughness improvements are calculated based on a comparison of the second- and first-order interlocking sutures, other studies[9,10,19] are presented based on a comparison of the first- and zero-order (i.e., bulk material) interlocking ones. In addition, some of the designs with the highest toughness improvement compared with their lower-order interlocking sutures (i.e., first- or zero-order interlocking) were reported in the selected studies.[4,9,10,19] It is seen that the current study has a comparable toughness improvement with the suture designs, materials, and manufacturing methods available in the literature. The mechanical properties of the bulk materials and interfaces in the studies were different, leading to different toughness improvements. Current suture designs can be used to tune the mechanical performance of ceramic systems.

4. Conclusions

Suture structures are widespread in nature and have gained popularity in engineered bio-inspired applications. Owing to their complexity, sophisticated structures in nature that have resulted from years of evolution can only be replicated using advanced and intelligent manufacturing technologies. To study the effectiveness of bioinspired structural architectures in engineered ceramic systems, a manufacturing platform was developed and a multimodal mechanical study was performed to characterize the tensile, flexural, and fracture mechanics of hierarchical suture ceramics. The developed near-net manufacturing system enables the precise, defect-free replication of bioinspired architectures with minimal material removal (to minimize the reduction in stiffness). These engineered interfaces contribute to the activation of energy dissipation mechanisms while ensuring geometric interlocking. In addition, the adhesive interlayer plays a significant role in toughness and stiffness tunability. Interlocking systems of two orders of the hierarchy were explored, with the anti-trapezoidal *N1* (5°, 15°, and 25°) and mixed-architecture ceramic sutures *N1-N2* (*N1*: 5°, 15°, and 25° and *N2*: 5°, 15°, 25°, and 35°). The effects of first- and second-order geometrical interlocking and different loading modes on the deformation and failure mechanics of ceramic sutures were experimentally investigated by examining their force displacement, stress–strain, and progressive failure responses. It is observed that the ceramic sutures with a second-order structural hierarchy offer substantial improvements in toughness by facilitating an enhanced interlocking, resulting in less brittle fractures. It was shown that the effective interlocking angles can make the pullout mechanism functional, resulting in a stable system in which the force progressively decreases with the crack opening. When comparing ceramic sutures with different geometrical hierarchical orders, second-order ceramic sutures demonstrate both higher strength and deformability. For first-order ceramic sutures, stiffness generally depends on the interface strength. In contrast, for second-order ceramic sutures, geometric interlocking and frictional interactions at weak interfaces also contribute to the stiffness and strength of the structures. Different failure mechanisms owing to differences in the locations of the stress and strain were captured using DIC. Under loading, the maximum strain was extensively concentrated along the weak interfaces, leading to structural interlocking caused by geometric interference. The deformation of the ceramic suture increased to the point where the teeth were either pulled out or fractured. The findings suggest that by adjusting the suture architecture, the toughness of ceramic systems can be greatly improved, even if the suture substrate is intrinsically brittle. This design strategy provides a new approach to developing architected ceramics with a wide range of engineering applications. By fine-tuning the geometric orientation (i.e., interlocking teeth), size (i.e., the order of hierarchy), and tile-cut features (i.e., curvature) of trapezoidal and elliptical morphologies in ceramic suture systems, a diverse design space can be created.

5. Experimental Section

Design: To develop an easy variable cut program, SolidWorks (Dassault Systems) was used to create a parametrically defined interface. The hierarchical teeth were a combination of anti-trapezoidal teeth at *N1*, with a 14 mm amplitude, and tangentially constrained ellipses with an aspect ratio of 1.8:1 and an amplitude of 2.6 mm at *N2* (inspired by

ADVANCED MATERIALS INTERFACES
Open Access
www.advmatinterfaces.de

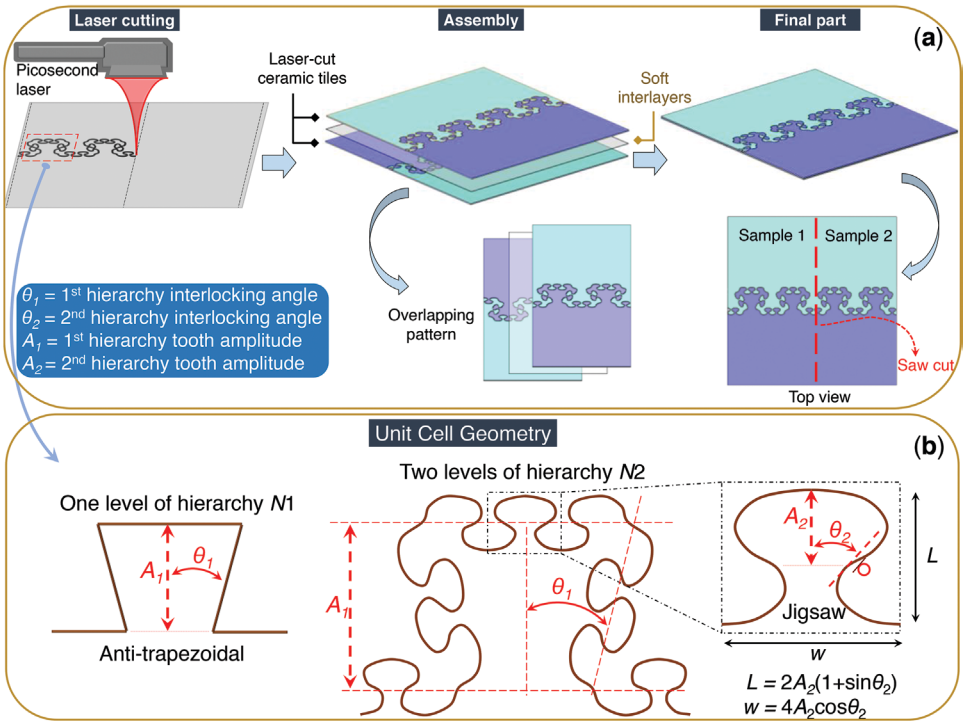

Figure 7. a) Manufacturing steps of the multilayered ceramic sutures: laser machining ceramic tiles and simplified lamination, and b) design and arrangement of material architectures: anti-trapezoidal and jigsaw.

the diabolical iron-clad beetle).[19] The amplitudes were chosen such that two samples could fit within a 114.3 mm wide square panel with a minimum of three full interlocking teeth per horizontal edge per length scale. Furthermore, a 1:1 *N1* tooth aspect ratio was used to fit four *N2* teeth on the anti-trapezoidal interlocking interface, resulting in 180° rotational symmetry. Therefore, the samples were denoted using θ_1-θ_2 nomenclature, where θ_1 (*N1*) is equal to 5°, 15°, or 25°, whereas θ_2 (*N2*) is 5°, 15°, 25°, or 35° (a design set surrounding the interlocking angle of 15° was chosen because this critical value was reported as the optimal angle for pullout without fracture). Amplitudes (A_1 and A_2) and interlocking angles (θ_1 and θ_2) at both length scales were used to define the geometry, with the interlocking angles serving as the variable parameters (see **Figure 7**). The 1.5-tooth unit cells of each geometry were exported in dxf file format to be imported directly into the IPGWeld processing software and patterned to create the 3-tooth suture.

High Precision Laser Machining of Ceramics: An ultra-short pulsed Ytterbium picosecond fiber laser (YLPP-25-3-50-R, IPG Photonics, USA) was used to engrave the designs on 0.635 mm thick alumina ceramic tiles, 114.30 × 57.15 mm^2 in overall dimensions (high-tolerance fired non-porous alumina ceramic with 96% material composition, a density of 3875 kg m^{-3}, and Modulus of elasticity of 303 GPa, McMaster-Carr) as shown in **Figure 8**. The laser unit produced a beam with a wavelength of 1030 nm with a Gaussian spatial profile (Figure 8d). The unit was operated at a maximum average power of 50 W, achieved via three picosecond-long pulses of 25 µJ each. A previously developed high-precision laser ablation procedure[34,35] was used to produce melting and recast-layer-free grooves in the substrate. The laser program was run for 175 passes, with the *z*-position being raised from 93.20 to 93.50 mm at 80 passes to ensure the Rayleigh range or vertical laser focus window did not limit cut efficiency. In previous works,[34,35] the impact of *z*-position on the cut efficiency and wobble amplitude on the cut depth was demonstrated. Notably, a wobble amplitude of 0.5 mm was required to cut to a depth of 0.635 mm. The processing time of a panel was ≈90 min for the samples exhibiting one order of hierarchy and 120 min for those with two orders of hierarchy owing to the longer path length.

Manufacturing: Once the tiles were laser-cut, a pair of identical geometries was laminated in an overlapping manner, with the wider cut width interface facing inward (rotated 180° with respect to each other, see Figure 7a). Surlyn was sandwiched between alumina tiles, which were then placed under vacuum in an oven for 5 h at 146 °C. Once removed, polymer infiltration was validated by the pattern left on the release film, in addition to microscopy of the cross-section. A circular diamond cut-off saw was then used to separate the two samples and trim the edges. The design choice to have overlapping geometries was driven by two factors: I) the overlapping design was critical for the bond strength at the joint when using the lamination method. Substrate adhesion at the joint interface ensures comprehensive polymer infiltration into the cuts without any voids or pitting, and II) the flexural stiffness offered by overlapping teeth was increased. At this thickness scale for the joint, the flexural interlocking provided by non-overlapping teeth was negligible, resulting in a test of the tensile strength of the ionomer only. In summary, because inspiration was taken from multiple joint types observed in nature rather than identically mimicking a joint found in nature, this was deemed to be the best approach.

Four-Point Bending Tests: Four-point bending samples 55 mm in width, 114.3 mm in height, and 1.6 mm in thickness were manufactured from overlapping alumina tiles with interlocked suture geometries composed of three full teeth and two half teeth. The samples featured a weak interface composed of thermoplastic Surlyn. 15 double-layer panels (*N1-N2* sutures), including *N1* suture samples as a baseline (Figure 8e), were tested in flexure by loosely adapting ASTM Standard C1161-18. The outer span of the bending fixture was set to 80 mm and its inner span was set to 40 mm. The loading rate was set to 0.2 mm min^{-1} with data acquisition occurring at a rate of 10 Hz to clearly capture the progressive failure of the samples. The width and thickness of each sample were measured at three locations and averaged to obtain the sample dimensions. Data analysis was performed using Python 3. The flexural stress of a sample whose inner span is half of its outer span was computed using Equation (1)

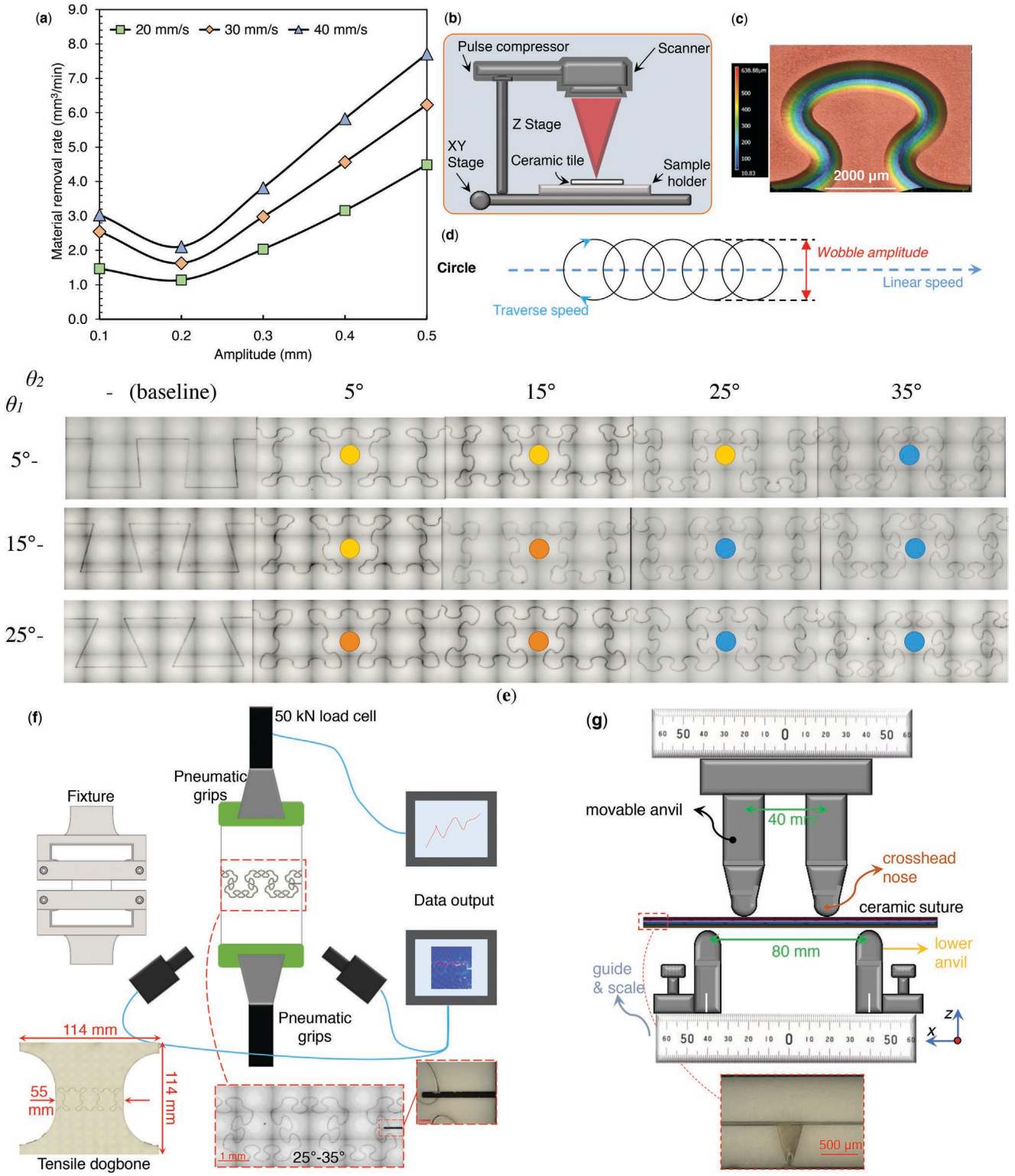

Figure 8. a) The material removal rate as a function of wobble amplitude at different linear speeds, b) the laser system and its equipment, c) 3D laser scanning microscopy image of a suture, and d) circular wobble pattern shapes and its parameters. e) Microscopy images of the samples where the *y*-axis corresponds to the *N1* interlocking angle, and the *x*-axis corresponds to the *N2* interlocking angle (the scale is 500 µm, *colors classify three types of corner teeth). Schematic diagram of f) tensile and fracture toughness testing, and g) Quasi-static four-point bending test. Optical microscopy of the cross-section (as well as marks on the release film following layup) offers sufficient evidence of complete polymer infiltration.

$$\sigma = \frac{3FL}{4bd^2} \quad (1)$$

where F is the load, L is the outer support span, b is the sample width, and d is the sample thickness. The UFS was extracted from the maximum of each stress–strain curve. Configuration C for four-point bending was used as a reference for the support and loading spans in the flexure. The tested samples stray from the standard in that their depth and width were much larger than those of typical test samples. Using this standard, Equation (1) provided the strength of a beam in four-point bending using the maximum load (break force). This equation typically considered the outer surface of the sample, where the maximum stress occurred. This formula can also be used to calculate the instantaneous stress in the loading region (between the inner rollers). However, because this sample was sufficiently thin, a constant stress assumption could be made over that region. This assumes a constant stress field, which was not the case with a jointed sample such as this, although the formula was assumed to still apply as the bulk properties were examined. The stiffness was computed by taking the slope of the curve for the first 100 s (linear region before any fracture) using the linear regression *SciPy* module in Python 3. The toughness was calculated using the trapezoidal rule module in *NumPy*. All analytical methods were validated using manual calculations.

Fracture Toughness Testing: The fracture toughness performance of all the samples was evaluated using methods loosely based on the ASTM-E399-20a standard for linear-elastic plane strain for metallic materials. The standard recommended a crack length to sample width ratio of greater than 0.2; however, a crack of length 8 mm with a minimum cut length (caused by circular blade cutting at an angle) of 6.2 ± 0.1 mm was used for these tests. The notch was cut with a Struers circular cut-off wheel equipped with a diamond saw blade with a thickness of 0.6 mm. A crack length of 8 mm gave a length-to-sample width ratio of 0.14, (0.008 m/0.057 m). The notch length was selected such that it would intersect the weak interface for all the samples. This was done so that the stress was channeled into the weak interface, and reliable failure in the notch region was guaranteed.[36] While this could certainly affect the nominal results, the comparison between different samples should remain valid. While this is outside the acceptable range for a representative test in the standard, it was assumed that for comparison purposes between similar samples, the disparate length-to-width ratio would not impact the analysis.

Samples identical to those tested in bending were notched using a Struers circular cut-off wheel equipped with a diamond saw blade (M0D31, Struers, Denmark) with a thickness of 0.6 mm. The notching distance had a consequent minimum cut length (caused by circular blade cutting at an angle) of 6.2 ± 0.1 mm. The green painter's tape was then wrapped around the top and bottom of the samples six times to counteract localized compression in the grips, causing a premature fracture at the grip site (serrated, 25×25 mm^2). Pneumatic grips (MTS Systems Advantage 2 kN Pneumatic Grip) were mounted on an MTS 50 kN load frame (810 Material Test System) using custom-machined adapters. The setup was self-aligned under tension to ensure rotational alignment. The pneumatic grips initially gripped the samples at 207 kN before increasing the pressure to 345 kN (25 mm^2 grips, 215 N grip force). Prior to testing, the samples were sprayed with a speckled black dot pattern for the DIC to track localized deformation, with image acquisition occurring at 2 Hz. The extension rate was set to 5 mm min^{-1} and the samples were loaded until failure, defined as edge-to-edge crack propagation.

ASTM E399 method A4 (compact specimens) was used for this application. The fracture toughness (K) was calculated using Equation (2)

$$K = \frac{P}{B\sqrt{W}} \times f\left(\frac{a}{W}\right) \quad (2)$$

where P is the critical load, B is the specimen thickness, W is the specimen width, a is the notch length, and $f(a/W)$ is the notch length.

$$f\left(\frac{a}{W}\right) = \frac{\left(2+\frac{a}{W}\right)\left[0.886+4.64\left(\frac{a}{W}\right)-13.32\left(\frac{a}{W}\right)^2+14.72\left(\frac{a}{W}\right)^3-5.6\left(\frac{a}{W}\right)^4\right]}{\left(1-\frac{a}{W}\right)^{\frac{3}{2}}} \quad (3)$$

Accurate within 0.5% for a/W ratios ranging from 0.2 to 1, with the tested samples having $a/W = 0.14$; thus, it was assumed to be within reasonable accuracy limits.

Tensile Testing: Blank dogbone samples of varying geometries were tested using a custom fixture to determine the geometry that would lead to failure in the gauge region, which was a major hurdle in the tensile testing of brittle materials. The dogbones had to be laser-cut from standard 114.30 mm square panels, which served as the major limitation of the design. Consequently, it was decided to use a 2-tooth (vs 4-tooth) design to achieve a sufficiently narrow-gauge region such that the samples would reliably fail in the gauge. Figure 8f illustrates the dimensions of the dogbone, as well as the final fixture and dogbone setup. The interface between the fixture and the sample was cushioned with a square silicone cord stock and secured in place using a Loctite 380 instant adhesive. This effectively prevented stress concentrations at the sample-fixture interface. The same MTS tensile testing machine used for fracture testing was used for tensile testing, with a 10 kN load cell installed to capture any progressive failure, which otherwise could be hidden by excessive noise caused by the hydraulic grips. Furthermore, a laser extensometer (2710-11T, Applied Tests Systems, Inc., USA) was used, as the reflective tape could be placed directly on the custom fixture for reliable strain results. The stress was calculated as $\frac{P}{bw}$, while the strain was calculated as $\frac{l-l_0}{l_0}$. The ultimate tensile strength was taken as the critical stress, and the slope of the first 500 data points of the stress–strain curve was used to calculate the stiffness. Energy absorption was calculated using NumPy's trapezoidal rule in Python, considering the area under the stress–strain curve.

Digital Image Correlation: A 3D DIC system was used during the tensile tests to measure the deformation of the ceramics (Figure 8f). The stereoscopic DIC system consisted of two high-speed cameras (Trilion Aramis Adjustable (2D) using GOM Image processing) set to capture images at two frames per second (fps) with a resolution of 12 megapixels (4096×3000 pixels). A stochastic speckle pattern was sprayed onto the ceramic surface using a black paint canister. The double-layer ceramic tile provided a natural white-colored background; hence, the maximum grayscale contrast could be achieved using black paint or ink. DIC data were analyzed using GOM Aramis version 6.3. By determining the correspondence between each of the deformed and reference subsets (regularized square regions), the full-field displacement over the area of interest can be calculated and then later differentiated to produce a full-field strain map for each of the test images. However, owing to significant crack nucleation and propagation throughout the area of interest during the tests, the strain data maps exhibited artifacts along and around the crack path, as the cracked region resulted in a fictitious strain. Thus, the strain data were only used for qualitative purposes to capture failure initiation and propagation throughout the specimens, whereas the displacement data were used for quantitative comparisons and analysis.

Data Analysis Methods: The fracture testing data were cleaned using a low-pass filter (implemented in Python 3) to counteract the noise generated by the 50 kN load cell. Adjustments were made to the testing apparatus to reduce noise, eliminating the need for post-processing of the tensile data. As the tensile samples were constrained in a fixture rather than directly gripped, the 10 kN load cell could be placed below the hydraulic grips of the apparatus, which was the major source of the noise.

Supporting Information

Supporting Information is available from the Wiley Online Library or from the author.

Acknowledgements

This research was funded by National Research Council Canada (NRC). The authors also acknowledge M. Gaudioso, W. Amsellem, and M. Guérin for their assistance with the data analysis and DIC performing.

Conflict of Interest

The authors declare no conflict of interest.

Author Contributions

Z.K.: Conceptualization; data curation; formal analysis; roles/writing – original draft; writing – review and editing. H.Y.: Data curation; formal analysis; investigation; methodology; project administration; resources; software; supervision; validation; visualization; roles/writing–original draft; writing–review and editing. J.G.: Funding acquisition; project administration; resources; software; validation; writing – review and editing. B.A.: Funding acquisition, project administration, resources; supervision; writing, review, and editing.

Data Availability Statement

The data that support the findings of this study are available on request from the corresponding author. The data are not publicly available due to privacy or ethical restrictions.

Keywords

digital image correlation, flexure, laser system, suture, tension, toughness

Received: March 8, 2023
Published online: April 7, 2023

[1] S. E. Naleway, M. M. Porter, J. McKittrick, M. A. Meyers, *Adv. Mater.* **2015**, *27*, 5455.
[2] A. R. Studart, *Adv. Mater.* **2012**, *24*, 5024.
[3] F. Libonati, *Adv. Eng. Mater. Model.* **2016**, *1*, 165.
[4] E. Lin, Y. Li, J. C. Weaver, C. Ortiz, M. C. Boyce, *J. Mater. Res.* **2014**, *29*, 1867.
[5] W. Wang, Y. Sun, Y. Lu, J. Wang, Y. Cao, C. Zhang, *J. Mech. Behav. Biomed. Mater.* **2021**, *113*, 104137.
[6] Z. Yu, J. Liu, X. Wei, *J. Mech. Phys. Solids* **2020**, *142*, 104010.
[7] R. Rakshit, A. K. Das, *Precis. Eng.* **2019**, *59*, 90.
[8] H. Y. Sarvestani, M. Mirkhalaf, A. H. Akbarzadeh, D. Backman, M. Genest, B. Ashrafi, *Mater. Des.* **2019**, *167*, 107627.
[9] I. A. Malik, F. Barthelat, *Int. J. Solids Struct.* **2016**, *97–98*, 389.
[10] M. Mirkhalaf, A. K. Dastjerdi, F. Barthelat, *Nat. Commun.* **2014**, *5*, 3166.
[11] T. Siegmund, F. Barthelat, R. Cipra, E. Habtour, J. Riddick, *Appl. Mech. Rev.* **2016**, *68*, 040803.
[12] T. P. Niebel, D. Carnelli, M. R. Binelli, R. Libanori, A. R. Studart, *J. Mech. Behav. Biomed. Mater.* **2016**, *60*, 367.
[13] Y. Zhang, H. Yao, C. Ortiz, J. Xu, M. Dao, *J. Mech. Behav. Biomed. Mater.* **2012**, *15*, 70.
[14] H. Y. Sarvestani, C. Beausoleil, M. Genest, B. Ashrafi, *Extreme Mech. Lett.* **2020**, *39*, 100844.
[15] A. Rahimizadeh, H. Y. Sarvestani, L. Li, J. B. Robles, D. Backman, L. Lessard, B. Ashrafi, *Mater. Des.* **2021**, *198*, 109375.
[16] H. Y. Sarvestani, M. Mirkhalaf, A. Akbarzadeh, D. Backman, M. Genest, B. Ashrafi, *Mater. Des.* **2019**, *167*, 107627.
[17] H. Y. Sarvestani, D. A. van Egmond, I. Esmail, M. Genest, C. Paquet, B. Ashrafi, *Adv. Funct. Mater.* **2022**, *32*, 2108492.
[18] I. A. Malik, M. Mirkhalaf, F. Barthelat, *J. Mech. Phys. Solids* **2017**, *102*, 224.
[19] J. Rivera, M. S. Hosseini, D. Restrepo, S. Murata, D. Vasile, D. Y. Parkinson, H. S. Barnard, A. Arakaki, P. Zavattieri, D. Kisailus, *Nature* **2020**, *586*, 543.
[20] I. H. Chen, W. Yang, M. A. Meyers, *Acta Biomater.* **2015**, *28*, 2.
[21] C. R. Jaslow, *J. Biomech.* **1990**, *23*, 313.
[22] N. Curtis, M. E. H. Jones, S. E. Evans, P. O'Higgins, M. J. Fagan, *J. R. Soc., Interface* **2013**, *10*, 20130442.
[23] H. E. White, J. Clavel, A. S. Tucker, A. Goswami, *J. R. Soc., Interface* **2020**, *17*, 20200476.
[24] Y. Li, C. Ortiz, M. C. Boyce, *Phys. Rev. E* **2012**, *85*, 031901.
[25] E. Lin, Y. Li, C. Ortiz, M. C. Boyce, *J. Mech. Phys. Solids* **2014**, *73*, 166.
[26] N. Lee, L. N. Williams, S. Mun, H. Rhee, R. Prabhu, K. R. Bhattarai, M. Horstemeyer, *Biomed. Phys. Eng. Express* **2017**, *3*, 035025.
[27] Z. Liu, Z. Zhang, R. O. Ritchie, *Acta Biomater.* **2020**, *102*, 75.
[28] Y. Cao, W. Wang, J. Wang, C. Zhang, *J. Mech. Behav. Biomed. Mater.* **2019**, *92*, 40.
[29] I. A. Malik, F. Barthelat, *Int. J. Solids Struct.* **2018**, *138*, 118.
[30] M. Mirkhalaf, F. Barthelat, *Extreme Mech. Lett.* **2017**, *11*, 1.
[31] K. Kohama, *Sci. Technol. Weld. Joining* **2020**, *25*, 383.
[32] M. Ksiazek, N. Sobczak, B. Mikulowski, W. Radziwill, B. Winiarski, M. Wojcik, *J. Mater. Sci.* **2005**, *40*, 2513.
[33] W. Zhu, H. Zhang, D. Xue, H. Jiang, X. Ran, *Ceram. Int.* **2019**, *45*, 20999.
[34] C. Beausoleil, H. Y. Sarvestani, Z. Katz, J. Gholipour, B. Ashrafi, *Ceram. Int.* **2020**, *46*, 15285.
[35] I. Esmail, H. Y. Sarvestani, J. Gholipour, B. Ashrafi, *Opt. Laser Technol.* **2021**, *135*, 106669.
[36] T. Nishida, Y. Hanaki, G. Pezzotti, *J. Am. Ceram. Soc.* **1994**, *77*, 606.